Nuclear Fusion

ACCEPTED MANUSCRIPT

Width and rugosity of the topological plasma flow structures and their relation to the radial flights of particle tracers

To cite this article before publication: L. García et al 2015 *Nucl. Fusion* ***55*** *113023*

https://doi.org/10.1088/0029-5515/55/11/113023

Width and rugosity of the topological plasma flow structures and their relation to the radial flights of particle tracers

L. García[1], I. Llerena Rodríguez[2] and B.A. Carreras[1]

[1] Departamento de Física, Universidad Carlos III de Madrid, Avda. de la Universidad 30, 28911 Leganés, Madrid, Spain
[2] Departament d'Àlgebra i Geometria, Facultat de Matemàtiques, Universitat de Barcelona, Gran Via de les Corts Catalanes, 585, 08007 Barcelona, Spain

E-mail: lgarcia@fis.uc3m.es, illerena@ub.edu and bacarreras@gmail.com

Abstract. Analysis of the distributions of width and rugosity of the topological plasma flow structures is presented for some resistive pressure-gradient-driven turbulence results. The distributions of the radial excursions of particle tracers during trappings are compared with those of the width and rugosity of the flow structures.

PACS numbers: 52.35.Ra, 52.65.Kj, 47.27.-i

1. Introduction

Turbulence induced transport is one of the outstanding physics problems in plasma physics [1]. In the turbulence induced transport issue, our long-term perspective is to proceed in three steps. First identification of turbulent flow structures using topological and geometric techniques and characterization of their statistical properties [3], [4]. Second, to relate these topological structures to properties of tracer particles within a framework of the continuous random walk (CTRW) approach [2]. Third, to construct a transport theory based on the CTRW approach and use the information we obtained in characterizing the tracer particle properties. We are working on the framework of the Resistive Magnetohydrodynamic (MHD) turbulence and we are now at the second step in the process, although we will have to go back to the first one to answer some of the questions that may emerge along this research. The MHD model used is discussed in section 2.

In the first step of our research, we used topological tools to characterize the flow structures [3], [4]. To study the structures of the $E \times B$ flows we use the electrostatic potential. To do so, we analyze the sets of points greater than a given value of the potential, some of the details are discussed in section 3. Here we are particularly interested in visualizing some of the relations between flows and tracer particles. So, in the case of cylindrical geometry, we use a coordinate transform that unscrews the helical structures in each radial position in such a way that all magnetic lines become parallel at the axis of the cylinder. Then the structures can be projected on a 2D toroidal cut. We will discuss the details of this transformation in section

3. In figure 1(a) we show an example of the flow structures at a fixed time. These projections appear as orange spots in this figure.

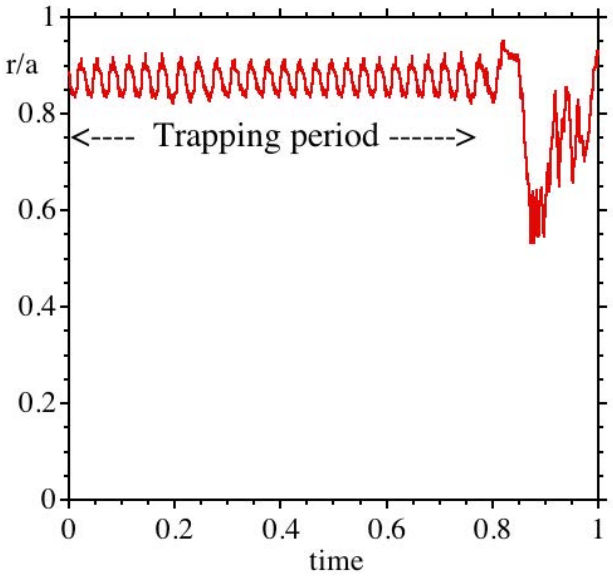

Figure 1. (a) Flow structures and tracer trajectory after applying the transformation and projecting on the $\zeta = 0$ plane for case 1. (b) The tracer trajectory with multiple trappings.

FIG1

The use of particle tracers has proven to be very helpful in trying to understand turbulence-induced transport in magnetically confined plasmas. Particle tracers have been used in numerical simulations to characterize diffusive transport [5], [6], [7] and also non-diffusive transport [8]. Now, we try to use this approach in relating the tracer orbits to flow structures.

When we look at tracer particle motion, we see that vortices may cause some of the trapping of particles, while large scale flows may carry them from vortex to vortex. This picture of the particle transport in plasma turbulence is consistent with the interpretation of the transport from the perspective of the CTRW. Here we interpret the tracer trajectories from this point of view.

First, we decompose the tracer trajectories in radial flights, i.e. radial intervals in between points where the radial velocity changes sign. A sequence of flights around the same radial point corresponds to a trapping, an example of simple trapping of a tracer trajectory is shown in figure 2; the rest of flights are jumps either between trappings or out of the plasma. These jumps also can have one or many flights. Of course, precise criteria for trappings are important and far from trivial. We will discuss them in section 5.

In this paper we focus on the characterization of the trappings and their relation to the geometrical properties of the flow structures. Therefore, we analyze mainly the tracer trajectories for a fixed turbulence configuration. We leave the relation between the trapping times and lifetimes of the flow structures and other detrapping mechanisms to a further phase in this research.

It is reasonable to think that trappings and flights are closely related to the

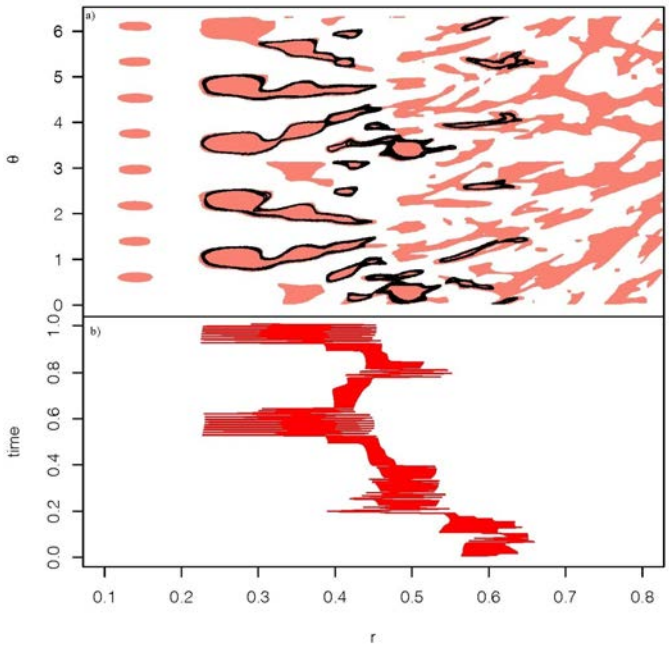

FIG2

Figure 2. Example of trapping on a tracer trajectory.

properties of the plasma flow. These radial excursions are relatively regular during the trapping period but they can vary a great deal from trapping to trapping as shown in figure 1(b). Since in many cases the tracer is captured by the turbulent vortices, we will study the relation between the width of the vortices and the radial flights of the particles during the trappings. Figure 1 illustrates the situation: a tracer is captured in succession by vortices with different widths so that the radial excursions of the corresponding trappings are also different.

However, that is not the only type of trappings that exist. In the case of the presence of an averaged poloidal flow, a kind of transport barrier forms [4] and tracer particles move along the surface of the barrier. The barriers do not have smooth surfaces; they have a degree of roughness. This roughness translates on radial motion of the tracer, so we need a way to describe its properties. To characterize the roughness, we introduce a rugosity coefficient. There are many definitions of such coefficients used in multiple disciplines, from Chemistry [9] to Ecology [10]. Since in our case the deformations of the surfaces are nearly periodic, we use one of the simplest definitions, the maximum variation of the surface in the direction perpendicular to the mean position of the surface. Details will be given in section 4. In figure 1(b), we can see how the tracer is going around several spots representing the flow structures. The correlation between trappings and the flow structures is clear from this figure.

The rest of the paper is organized as follows. After describing the turbulence model used in these calculations in section 2, we determine and characterize the flow structures and classify them, as it is discussed in section 3. In section 4, we show the determination of the width of the topological flow structures and calculate their statistical distribution under several conditions. In this same section, we discuss the

rugosity of the flow barriers and we also determine their statistical distribution. In section 5, we will compare the distribution of radial flights for sets of particle tracers and the distribution of the vortices width and barrier rugosity. The conclusions will be presented in section 6.

2. Resistive pressure driven model

sec:PlasmaModel

In this section, we describe the MHD model equations that we use in calculating the turbulent flows generated by resistive pressure-gradient-driven turbulence that are analyzed in this paper. We study the pressure-gradient-driven turbulence in cylindrical and toroidal geometry by means of a reduced set of resistive MHD equations [11] in the electrostatic limit [12]. For most of the cases considered, the geometry is that of a periodic cylinder, with minor radius a and length $L = 2\pi R$. We also compare results with a toroidal geometry case. In this section we describe the equations for the toroidal geometry. The changes when we go to the cylindrical geometry are straightforward.

We use a coordinate system (ρ, θ, ζ), in which ρ is either the normalized minor radius r for the cylindrical case, or a radius-like equilibrium flux surface label for the toroidal case, θ is the poloidal angle and ζ is either the toroidal angle for the toroidal case, or $\zeta = z/R$, where z is the coordinate along the axis of the cylinder, for the cylindrical case. The $E \times B$ velocity is written in terms of the electrostatic potential:

$$\mathbf{V}_\perp = -\frac{\nabla \mathbf{\Phi} \times \mathbf{b}}{\mathbf{B}} \tag{1}$$

Vperp

where Φ is the electrostatic potential, $\mathbf{B}$ is the magnetic field, and $\mathbf{b}$ is a unit vector in the direction of the magnetic field.

The model consists of two equations, the perpendicular momentum equation for the electrostatic potential evolution, and the equation of state for the pressure evolution. The first one is

$$m_i n_i \frac{d\tilde{U}}{dt} = -\mathbf{B} \cdot \nabla \left(\frac{R^2}{\eta F^2} \mathbf{B} \cdot \nabla \tilde{\Phi} \right) + 2 \frac{\mathbf{b} \times \boldsymbol{\kappa}}{B} \cdot \nabla \tilde{p} + m_i n_i \hat{\mu} \nabla_\perp^2 \tilde{U} \tag{2}$$

eq:U

Here, $d/dt = \partial/\partial t + \mathbf{V}_\perp \cdot \nabla$ is the convective derivative, $U = \boldsymbol{\zeta} \cdot \nabla \times \mathbf{V}_\perp / B$ is the toroidal component of the vorticity, η is the resistivity, $\boldsymbol{\kappa} = \mathbf{b} \cdot \nabla \mathbf{b}$ is the magnetic field curvature, and $\hat{\mu}$ is the viscosity coefficient. The magnetic field is expressed as $\mathbf{B} = F \nabla \zeta + \nabla \zeta \times \nabla \psi$, where $F = R B_\zeta$ is the toroidal flux function and ψ is the poloidal flux. The derivative along the magnetic field can be expressed as

$$\mathbf{B} \cdot \nabla = \frac{F}{R^2} \left(\frac{\partial}{\partial \zeta} - \frac{1}{q} \frac{\partial}{\partial \theta} \right) \tag{3}$$

Bgrad

where q is the safety factor, and R is the major radius. In cylindrical geometry, R and F are constant.

The equation of state for the pressure evolution is

$$\frac{d\tilde{p}}{dt} + \Gamma p \nabla \cdot \mathbf{V}_\perp = D_\perp \nabla_\perp^2 \tilde{p} + D_\parallel \frac{R^2}{F} \mathbf{B} \cdot \nabla \left(\frac{R^2}{F} \mathbf{B} \cdot \nabla \tilde{p} \right) \tag{4}$$

eq:pr

In equations (2) and (4), a tilde identifies perturbed quantities. For the nonlinear calculations, the effect of the $V_\parallel$ evolution in the dynamics of the resistive pressure-gradient-driven turbulence is replaced by a parallel diffusivity in the pressure equation. Viscosity and perpendicular transport are also included in the equations to provide the energy sink needed to get steady-state turbulence.

The driving term of the resistive pressure driven instability is the pressure gradient in the bad curvature region, that is, the second term on the right-hand side (rhs) of equation (2). The first term on the rhs is the field line bending term, which is stabilising. The resistivity weakens this term and allows the instability to grow.

In equation (2), the viscous term of the rhs for the $(m = 0, n = 0)$ component is a viscous drag $-m_i n_i \mu \tilde{U}_{00}$ due to magnetic pumping. In equation (4), an energy source term is added to the rhs for the $(m = 0, n = 0)$ component in order to compensate for dissipation and get a steady state.

In determining the solution of the equations, we use the following Fourier expansions:

$$\Phi(\rho,\theta,\zeta,t) = \sum_{m,n} \Phi^s_{mn}(\rho,t)\sin(m\theta+n\zeta) + \sum_{m,n} \Phi^c_{mn}(\rho,t)\cos(m\theta+n\zeta) \tag{5}$$

$$p(\rho,\theta,\zeta,t) = \sum_{m,n} p^s_{mn}(\rho,t)\sin(m\theta+n\zeta) + \sum_{m,n} p^c_{mn}(\rho,t)\cos(m\theta+n\zeta) \tag{6}$$

As discussed in Ref. [4], when no average poloidal flow is present, the solution is such that $\Phi^c_{mn}(\rho,t) = p^s_{mn}(\rho,t) = 0$. In this case, the function Φ has up-down symmetry $\Phi(\rho,-\theta,-\zeta) = -\Phi(\rho,\theta,\zeta)$. When an averaged poloidal flow is present, the averaged poloidal flow velocity, $\langle V_\theta \rangle$, is given by

$$\langle V_\theta \rangle = \frac{1}{B}\frac{d\Phi^c_{00}}{d\rho}. \tag{7}$$

To control the amount of average poloidal flow, we vary in the present calculations the value of the viscosity coefficient μ for the averaged flow. In what follows we will consider the results for four different types of plasmas. The four cases considered are listed in Table 1. All four cases correspond to low beta plasmas well bellow the ideal MHD stability limit. Details of the plasma parameters are given in Appendix A.

Table 1. The four plasma models discussed in this paper

Case	Geometry	Configuration	μ
1	Cylindrical	Stellarator	∞
2	Cylindrical	Stellarator	$50\tau_R^{-1}$
3	Cylindrical	Stellarator	$5\tau_R^{-1}$
4	Toroidal	Tokamak	∞

For each of the cases listed in Table 1, we calculate the evolution of the turbulent fields till reaches a steady state turbulence regime. Then during the steady state period, we analyze the function Φ at different times to determine the flow structures using the techniques described in the next section.

3. Topological structures of the turbulent flow

sec:TopolStruct

As we have already described in [3], [4], to study the topological structures of the turbulent flow we work with the electrostatic potential Φ. All the information on the turbulence is contained in the function Φ, as can be seen from equation (1). For instance, turbulence vortices can be easily identified by looking at the contours of the

function Φ. In what follows we will study the topological properties of this function, the method is explained in more detail in [3], [4].

In the previous studies [4] and at a fixed time t, we have defined a flow structure Ω as the set of points such that $\Phi(\rho,\theta,\zeta,t) \geq \Phi_0 \mathrm{Max}\Phi$ and $\Phi(\rho,\theta,\zeta,t) \leq \Phi_0 \mathrm{Min}\Phi$, where $0 < \Phi_0 < 1$.

As we discussed in [3], if we look at these flow structures in the case $\langle V_\theta \rangle = 0$, we can see that they are filamentary. This filamentary structure is due to the vortices of the turbulence resonating with the low singular surfaces. In those analysis, we found two basic types of structures: cycles and broken filaments.

In previous studies [3], [4] and in order to have enough space resolution, we study the structures on 2-D radial slices of the initial set Ω that we obtain by considering the subset of points $(\theta,\zeta) \in [0,2N) \times [0,N)$ such that

$$\begin{aligned} &\Phi(\rho, 2\pi\theta/2N, 2\pi\zeta/N, t) \geq \Phi_0 \mathrm{Max}\Phi \\ &\Phi(\rho, 2\pi\theta/2N, 2\pi\zeta/N, t) \leq \Phi_0 \mathrm{Min}\Phi \end{aligned} \tag{8}$$

eq:cubes

for constant values of ρ and t. For each time we take $2N$ values of ρ equally distributed in the interval $[0,1]$. Here, we take for most of the results $N = 300$. In [3], we found this level of resolution to be good enough for this studies and there we described some of the convergence studies using different values of N. We have used these subsets to study some of the topological properties of the flow structures.

Here and in order to gain information on the radial width of the flow structures, for each set of points Ω, we consider 2-D subsets corresponding to ζ = constant. That is, each subset is a constant toroidal angle cut of the set defined by the points $(\rho,\theta) \in [0,2N) \times [0,2N)$ such that

$$\begin{aligned} &\Phi(\rho/2N, 2\pi\theta/2N, \zeta, t) \geq \Phi_0 \mathrm{Max}\Phi \\ &\Phi(\rho/2N, 2\pi\theta/2N, \zeta, t) \leq \Phi_0 \mathrm{Min}\Phi \end{aligned} \tag{9}$$

eq:cubes1

for constant values of ζ and t. In figure 3, we show examples for the four cases of Table 1.

In each of these toroidal cuts, we identify the connected components following the same approach as we did for the radial slices in [3] and we determine the radial extend of each of them. These connected components are the topological flow structures that we discuss here. Note that they can be identified with one or more flow vortices. The trapped tracer trajectories are linked to the flow structure not to the individual vortices.

In the cylindrical geometry cases, to visualize the topological flow structures and to compare them with the particle tracer orbits, we do first a transformation of the poloidal angle θ to

$$\theta \to \theta + \zeta/q(r) \tag{10}$$

theta1

With this transformation, we unscrew the helical structures in such a way that the magnetic field lines became parallel at the axis of the cylinder. Then we can project the structures on the $\zeta = 0$ plane. We can represent this projection in the plane (r,θ); this will give spots that show the maximum width of the structures on the whole ζ range.

Figure 1(a) is an example of the projected structures for $\Phi_0 = 0.1$ at a fixed time for case 1 of Table 1. One can see structures of all sizes and shapes. Figure 4(a) shows the structures for $\Phi_0 = 0.1$ and for case 2. In this case, we can see these continuous

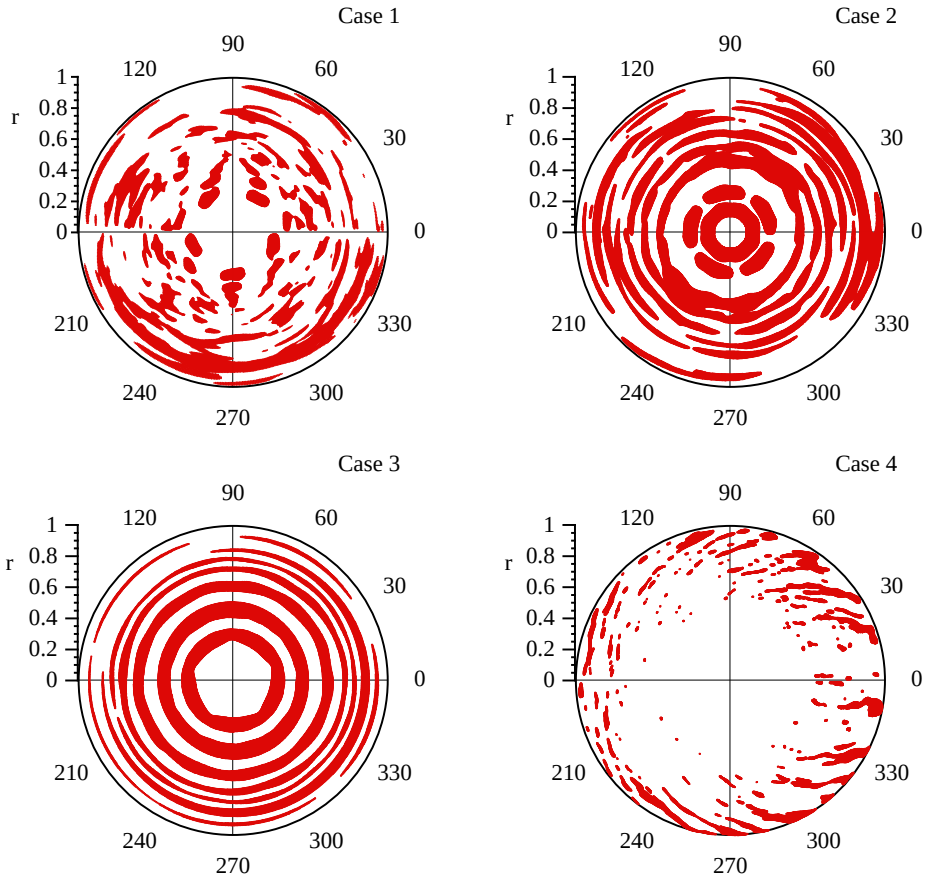

FIG3

Figure 3. Flow structures at the $\zeta = 0$ toroidal cut for a fixed time in the evolution for the four cases listed in Table 1.

structures in θ, they are the mini-transport barriers created by the shear flow, which were discussed in detail in [4]. They are particularly clear at small values of r.

Figure 1(a) also shows the projection of the tracer trajectory in Figure 1(b) that is trapped at different structures. This is the typical type of trapping for cylindrical geometry cases without an averaged poloidal flow.

Figure 4(a) shows the projection of three tracer trajectories on top of the flow structures. The one in blue (left), the tracer is trapped in a mini-transport barrier and remains there all time. The one in green (right), the tracer is trapped by a vortex structure. The third one in black (centre) is a kind of hybrid trajectory combining features of the other two. These are the typical types of trapping that happens in the case that there is an averaged poloidal flow.

For the cases that trapping is by a vortex structure, we expect the radial excursion of the tracer be directly related to the width of this vortex. However, in the case that the tracer is trapped by a barrier, the radial excursions are given by what we can call the rugosity of the barrier.

There are many ways to quantify the roughness of a surface. In general, it is used the rugosity parameter which is defined in different ways depending on the nature of

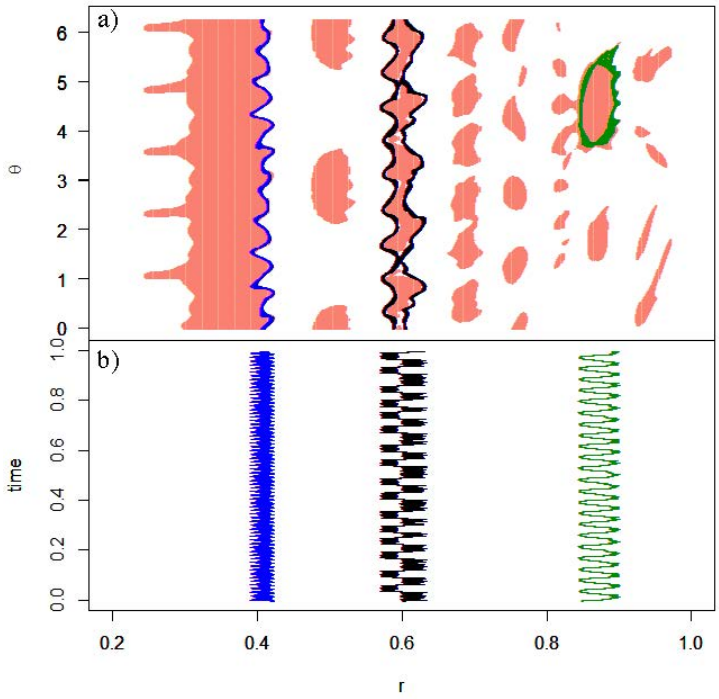

Figure 4. (*a*) Flow structures and three trajectories after applying the transformation of equation (10) and projecting on the $\zeta = 0$ plane for case 2. (*b*) The three trapped tracer trajectories.

FIG4

the roughness. Here we use the simplest way, the maximum variation of the surface in the perpendicular direction, which in this case is the radial direction. So, we define the rugosity of the transport barrier as

$$f_r = r_{max} - r_{min} \tag{11}$$

rugos

where r_{max} and r_{min} are the maximum and minimum values of the radius as we move along the barrier in the poloidal direction.

Now, having the two measures we want to use, the width of the filaments and the rugosity of the surface, we can study their probability distributions associated with the structures of the flows for the four cases from Table 1. This is done in the next section.

4. Probability distribution of the width of the flow structures

sec:ProbDistr

The radial extend of the connected components is taken as a measure of the radial width of the flow structure at a given time for a value of Φ_0 and in a given toroidal cut. This is done for all the toroidal cuts in such a way that we can make a set of the widths of the flow structures for statistical study.

From transport perspective it is important to characterize well the tail of the distribution functions. Since the number of flow structures at a given time is not very large, the probability distribution function (PDF) of these widths is in general noisy. However, it is always possible to work with the Rank function, that is 1 minus the

cumulative distribution function. The advantage is that to construct this function one does not use binning and all points of the sample are points of this function. So, the tail of the Rank function is better defined than the one of the PDF and we have better resolution. The consistency of the two fits, to the PDF and to the Rank, is an added constraint. In figure 5, we show an example of a PDF and a Rank function for the cylindrical geometry case without averaged poloidal flow, case 1 in Table 1. The data in this figure has been obtained from $N = 300$ equally spaced toroidal cuts for each of the 9 values of Φ_0, equally spaced from 0.1 to 0.9, used in this analysis.

In the case shown in figure 5, the distribution of widths seems to be well described by a lognormal distribution. The PDF of a lognormal is

$$P(W) = \frac{1}{W\sigma\sqrt{2\pi}} \exp\left[-\frac{(\ln W - \mu)^2}{2\sigma^2}\right] \tag{12}$$

lognorpdf

and the corresponding Rank function is

$$R(W) = \frac{1}{2} - \frac{1}{2}\,\mathrm{erf}\left(\frac{\ln W - \mu}{\sqrt{2}\sigma}\right) \tag{13}$$

lognorrank

Here, μ and σ are the mean and standard deviation of the width natural logarithm, respectively.

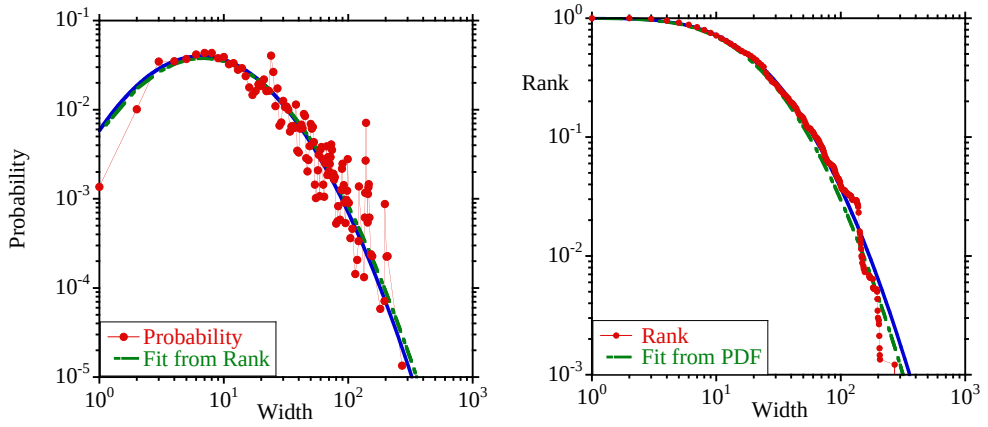

FIG5

Figure 5. PDF (left) and Rank (right) for the cylindrical geometry case without averaged poloidal flow at a fixed time.

In figure 5, at the left, we plot the PDF of the flow structure width for case 1 together with a fit (continuous line) by equation (12). The broken line gives the results of equation (12) using the parameters obtained by fitting the Rank function with equation (13). On the right panel of figure 5, we plot the Rank function together with a fit (continuous line) by equation (13) and the result from the same equation using the parameters obtained by fitting the PDF with equation (12). We can see that either fitting the PDF or the Rank function we obtain very similar results and both fits give a very good description of the data. The results are not sensitive to the way and number of values of Φ_0 selected.

It is interesting to note that the lognormal distribution describes most of the data analyzed from the flow structures. Here we have seen the distributions of the radial width and in [3] we obtained also a good description of the length of the flow filaments and the lifetime of the cycles.

To test the robustness of the results and to study the time variation of the structures, we have repeated the calculation for a fixed value of $\Phi_0 = 0.1$ and taking 20 different times for the same case 1 of Table 1. The results are shown in figure 6 using the same conventions as in figure 5.

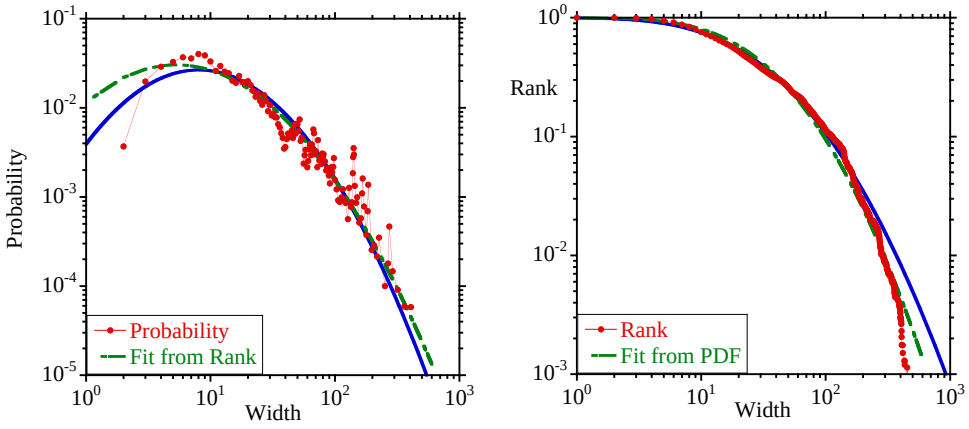

Figure 6. PDF (left) and Rank (right) for the cylindrical geometry case without averaged poloidal flow during time evolution for a fixed $\Phi_0 = 0.1$.

FIG6

Again we see in figure 6 the consistency between the fits to the PDF and Rank function. The parameters of the fit are also consistent with the ones in figure 5, within the error bars of the fits.

In case 2 from Table 1, there are two types of flow structures, as can be seen in figure 3. One type is like the ones in case 1, single o combined vortex structures. However there are also structures that poloidaly close on themselves. They are the mini transport barriers discussed in [4]. When we do the analysis of the connected components as done in case 1, we do not include the widths of the mini barriers, because the trapping of the tracers by these mini barriers is very different than the trapping by the other flow structures as we have shown in section 3.

The results of the analysis of the radial width for case 2 are shown in figure 7. In this figure we have plotted the PDF and Rank function of the radial width of the flow vortex structures.

Figure 7 is similar to figure 5, but in the present case we can see that the tail of the distribution falls off faster than the case with no averaged poloidal flow. This is probably a consequence of the shearing suppression effect [13] of the poloidal flow that breaks many of the turbulent flow structures and reduces their size.

In the case 2, there has also been a reduction on the number of flow structures, because of the shear suppression effect. That makes the PDF noisier. The situation gets even worse for case 3 of Table 1. In this case, the number of connected components, which are not mini barriers, is so small that is not possible to construct a reasonable PDF. This is a very extreme case in which most of the tracer particles are trapped by the shear flow. The Rank function for the width of the flow structures of case 3 is plotted in figure 8. We can see that the fall off of the tail of the rank function is even sharper than case 2.

Table 2 summarizes the cases with cylindrical geometry. We can see that the effect of the shear flow suppression of the turbulence is double. One is to reduce the

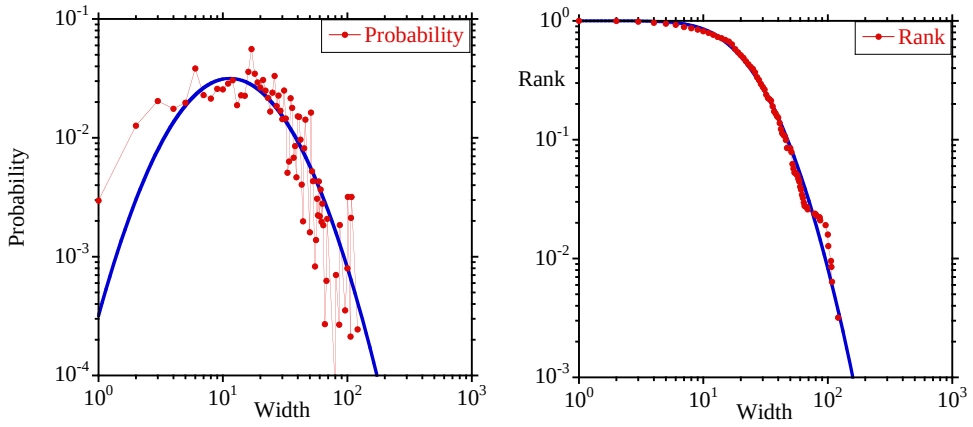

Figure 7. PDF (left) and Rank (right) for the cylindrical geometry case with averaged poloidal flow, case 2, at a fixed time.

FIG7

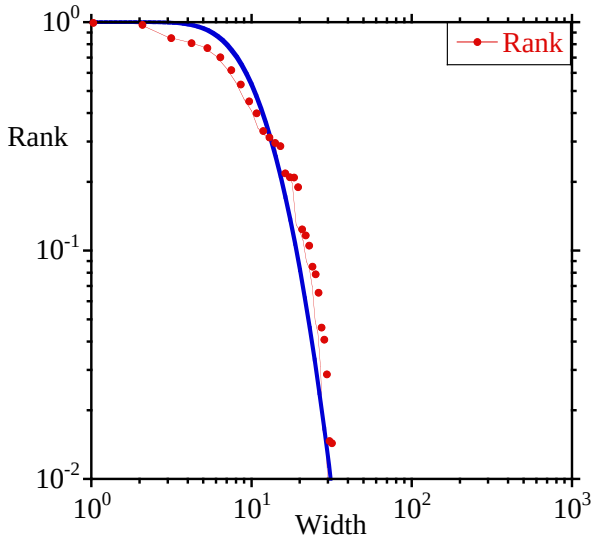

Figure 8. Rank for the cylindrical geometry case with averaged poloidal flow, case 3, at a fixed time.

FIG8

number of localized flow structures as we commented before. The other is to reduce the width of the remaining ones as shown by the change in parameters of the lognormal distributions.

Table 2. Fit to a lognormal distribution

	PDF		Rank	
Case	μ	σ	μ	σ
1	3.24	1.12	3.10	1.38
2	3.07	0.80	3.00	0.66
3			2.34	0.47

When we go to case 4 from Table 1 the dynamical situation changes. For all first three cases the underlying instability driving the turbulence is the resistive interchange mode. This is the typical case of the stellarators. However, in going to a tokamak the dominant instability is the resistive ballooning mode. The structure of the flows changes as can be seen in figure 3 and we could expect also changes in the width distribution.

In figure 9(a), we have plotted the PDF of the width of the flow structures for the case 4 at a fixed time and for 9 values of Φ_0, equally spaced from 0.1 to 0.9 (case 4a of Table 3) and in figure 9(b) the PDF of the width for $\Phi_0 = 0.1$ and varying time (case 4b of Table 3). The data for this case has been obtained from $N = 600$ toroidal cuts.

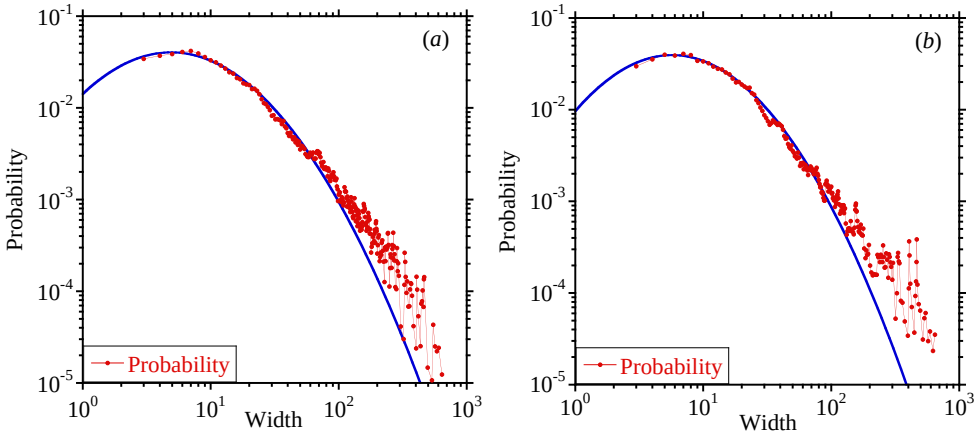

Figure 9. (a) PDF at fixed time and varying Φ_0 and (b) PDF for $\Phi_0 = 0.1$ and varying time for case 4, with a lognormal fit.

FIG9

The results are not quite consistent with a lognormal fit distribution. In looking at the tail of the PDF, they seem to show a possible power law fall off. To see if they are consistent with a power law, we apply the Clauset approach [14], which uses the consistency between the PDF and Rank function and makes a determination of the low boundary value where the power law starts. The results of applying this method to the two PDFs on figure 9 are given in Table 3. They can be compared with the same test for the PDF of case 1 in figure 5.

Clauset uses the criterion that the function is consistent with a power law if the parameter p is greater than 0.1. Clauset defines in [14] the parameter p as the probability that a data set of the same size as our data and that is truly drawn from the hypothesized distribution would have a goodness of fit as bad or worse than the observed value.

Table 3. Parameters from the fit by a power law

Case	α	W_{min}	p
4a	1.94	19	0.16
4b	1.87	13	0.16
1	3	109	0.06

In Table 3, α is the power law exponent, W_{min} is the lower limit of the power law range and p is the Clauset parameter.

The results shown in Table 3 seem very clear. For the toroidal geometry case there is consistency with a power law tail with an exponent close to 2 and a range of values for the width of more than a decade. However for case 1 that is not the case, the range of a possible power law is very small and p is less that 0.1. So the conclusion seems to be that the width distribution is consistent with a lognormal distribution for the cylindrical geometry cases and with a power law tail with exponent close to 2 for the toroidal case.

5. Tracer trajectories and flow structures

sec:TracerTraj

Having studied the statistical properties of the width of the flow structures for different geometries and global flow conditions, we can now study the statistical properties of the radial displacements of tracer particles during a trapping period when they are moving in the same turbulent flow fields that we have considered in the previous section.

Using the velocity fields obtained from the resistive pressure-gradient-driven turbulence calculations discussed in [3], we have studied the evolution of tracer particles. The velocity field perpendicular to the magnetic field is given in terms of the electrostatic potential, $\Phi(\rho, \theta, \zeta, t)$, by equation (1). Then the evolution of the tracers is given by

$$\frac{d\mathbf{r}}{dt} = -\frac{\nabla\Phi \times \mathbf{b}}{B} + V_0\mathbf{b}, \tag{14}$$

eq:tracer

where $\mathbf{r} \equiv (\rho, \theta, \zeta)$ is the tracer position, and V_0 is a constant velocity along the magnetic field lines. In solving this equation we can take Φ at a fixed time and use the frozen field or we can take Φ to be a function of time and then we have a dynamical evolution of tracers. Here, in order to understand better the relation between flow structures and tracer transport, we follow the first option.

ODE [15], a software integration package, is used to integrate equations (14) for given $\rho(\zeta_0)$ and $\theta(\zeta_0)$. ODE uses a modified divided difference form of the Adams-PECE formulas and local extrapolation. It adjusts the order and stepsize automatically. Note that in equations (14), since a Fourier series expansion is used for the angle variables θ and ζ, only onedimensional interpolation is required. Taking random initial condition in the whole cylinder, we follow the trajectory of 10^5 tracers till the end of the calculation and accumulate the data. This data is analyzed to identify the portion of the trajectories that the tracers remain trapped. We first look for tracers that are trapped during the full length of the calculation. We start by collecting the radial component of the left and right ends of the flights, $\{\rho_{li}\}$ and $\{\rho_{ri}\}$, respectively. We define the radial width of the trajectory as $\Delta\rho = \max_i\{\rho_{ri}\} - \min_i\{\rho_{li}\}$. Then, we go through the following steps, if needed.

(i) We calculate the standard deviation of the sets $\{\rho_{li}\}$ and $\{\rho_{ri}\}$. If both deviations are less than $0.05\Delta\rho$, we have a trapping for the whole trajectory.

(ii) If condition i is not met, we calculate the local maxima of right ends and the local minima of left ends. If the standard deviation of the sets of local maxima and local minima are less than $0.02\Delta\rho$, we have a trapping for the whole trajectory.

(iii) If condition ii is not met, we sort the local minima (maxima) and we select the smallest (largest) values until the next one is one or two points close to one of the local minima (maxima) already selected. Then, we calculate the average and standard deviation of the temporal separations between the minima and maxima selected. If both deviations are less than 10% of the corresponding average, we have a trapping for the whole trajectory.

The three conditions are chosen to ensure periodicity in the whole trajectory. In figure 10, we plot three examples of trajectories corresponding to a single trapping, verifying condition (i), (ii) and (iii), respectively. Small dots correspond to the left and right ends of flights, and big dots to the local maxima and minima.

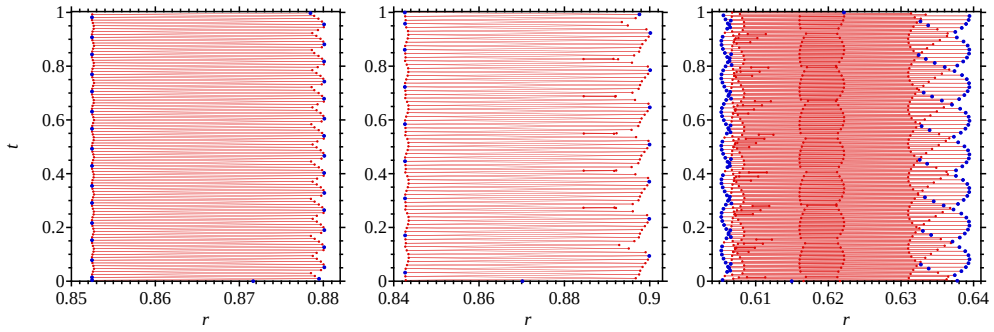

Figure 10. Three trajectories with a single trapping, verifying condition i (left), ii (middle) and iii (right) of the main text. The geometry is cylindrical and $\langle V_\theta \rangle \neq 0$ with $\mu = 50\tau_R^{-1}$.

FIG10

If there is more than a single trapping, we calculate for each local maxima (minima) the averaged radius of the part of the trajectory between that local maxima (minima) and the next one. We define a trapping as a set of consecutive maxima (minima) such that the difference of averaged radius between two successive maxima (minima) is less than 5% of the radial width of the portion of the trajectory defined by the set of maxima (minima). The radial width of a portion of the trajectory is defined in the same way we did for the whole trajectory. In figure 11, we show a trajectory with several trappings. The horizontal lines indicate the separation between trappings.

During the trapping time, we calculate the mean value of the radial flights of the tracers, $\langle \delta\rho \rangle$, and we construct the PDF of $\langle \delta\rho \rangle$ for different values of the parallel velocity V_0 to compare with the PDF of the width of the structures to see if they are related.

We first look at case 1 for a frozen flow situation. For each of the trappings, we also average the value of Φ during the trapping period, $\langle \Phi \rangle$. Since the tracers are initially at random locations, it is logical that the number of tracers trapped at a given value of Φ is proportional to the number of structures at this value of Φ. In figure 12, we can see that the distribution of the values of $\langle \Phi \rangle$ during the trappings is very similar to the distribution of the number of connected components of Φ associated with the structures identified trough the toroidal cuts, as discussed in section 3.

For case 1, the corresponding PDFs of $\langle \delta\rho \rangle$ for five values of the parallel velocity are plotted in figure 13(a).

From figure 13(a), the conclusion is that the PDF of $\langle \delta\rho \rangle$ is statistically independent of the parallel velocity. This is a general result for all cases considered

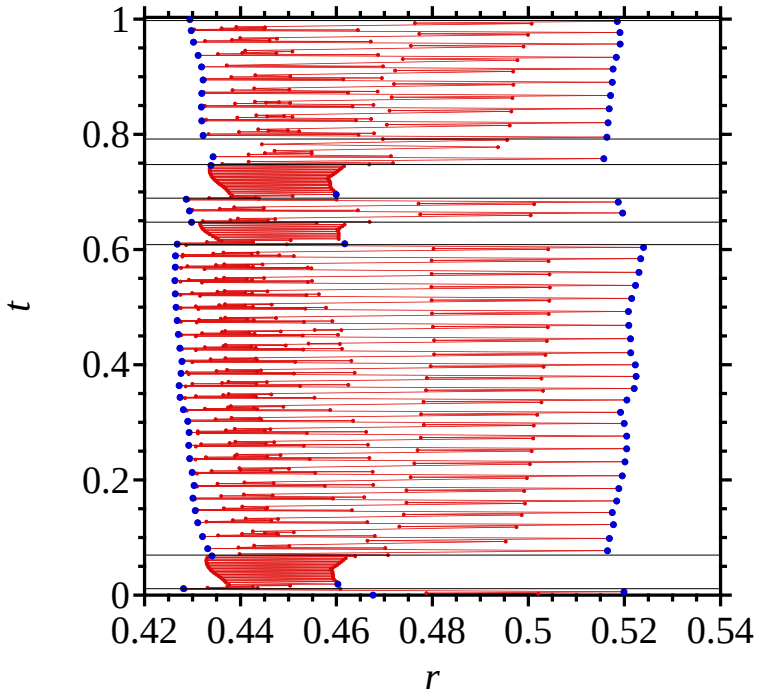

Figure 11. Trajectory with several trappings. Horizontal lines indicate the separation between trappings. The geometry is cylindrical and $\langle V_\theta \rangle \neq 0$ with $\mu = 50\tau_R^{-1}$.

FIG11

here and it is not a surprising results.

We have also considered the evolution of tracers in the evolving turbulence, during the same steady state period as we studied the flow structures and using the same turbulent flow field. For the integration of equations (14), we use the same integration package as in the case of fixed turbulence. Since each Fourier component depends now on ρ and t, bicubic interpolation for each Fourier component is required. The PDF of $\langle \delta\rho \rangle$ is very similar to the case of the frozen field evolution. In general, we have a smoother PDF for the evolving turbulence because of the varying conditions of the flow on one hand and also during the evolution tracers remain trapped for shorter times and the statistics are better than the case of the frozen turbulence. An example of the PDF is shown in figure 13(b), where it is compared with the PDF for the frozen field case and the PDF of the width of the flow structures. We can see that both PDF of $\langle \delta\rho \rangle$ are very similar to the PDF of the width of the flow structures.

When we go to cases 2 and 3 of table 1, we must group the trappings in two different groups. As we discussed in the previous section, when the average flow is present the trappings are of two types: by vortex structures and by barriers. To distinguish between the two types of trappings we measure the pitch q_p of the averaged tracer trajectory in the (θ, ζ) plane during the trapping. For the tracers trapped in flow structures, this pitch should be equal to $q(r)$, where q is the safety factor at the corresponding radial position. We use the condition

$$q_p + q(r) < c, \tag{15}$$

qcond

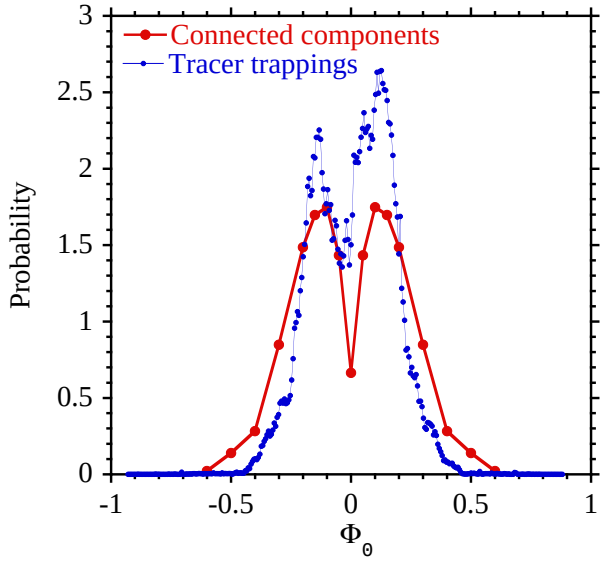

Figure 12. Comparison of the distributions of the number of connected components of Φ and of the averaged value of Φ during trappings.

FIG12

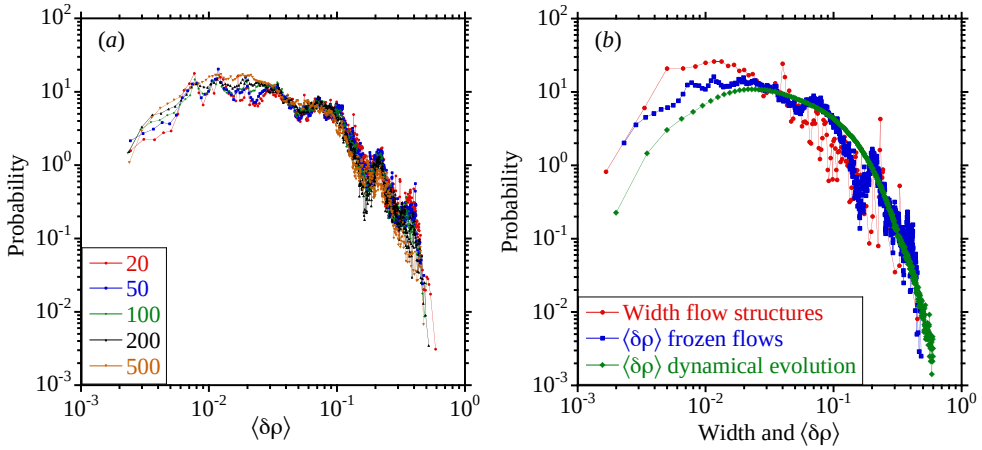

Figure 13. (*a*) PDFs of the $\langle\delta\rho\rangle$ of the tracers for five values of the parallel velocity, (*b*) PDF of $\langle\delta\rho\rangle$ for $V_0 = 200$ (frozen and evolving fields) and the PDF of the width of the flow structures for case 1.

FIG13

with c a constant to determine which tracers are trapped on the vortex structures. The constant c is taken to be a few percents of the value of q.

For case 2, we have plotted in figure 14(a) the PDF of $\langle\delta\rho\rangle$ for the tracers for frozen and evolving turbulent fields, both verifying the condition in equation (15) and the PDF of the width of the structures for this same case. In figure 14(b), we have plotted the PDF of $\langle\delta\rho\rangle$ for the tracers not verifying the condition in equation (15) and the PDF of the rugosity of the barriers for this same case 2.

We can see again in figure 14 a good agreement between radial structures of the flow and the $\langle\delta\rho\rangle$ of the tracers. Similar results are obtained for case 3, but the PDF

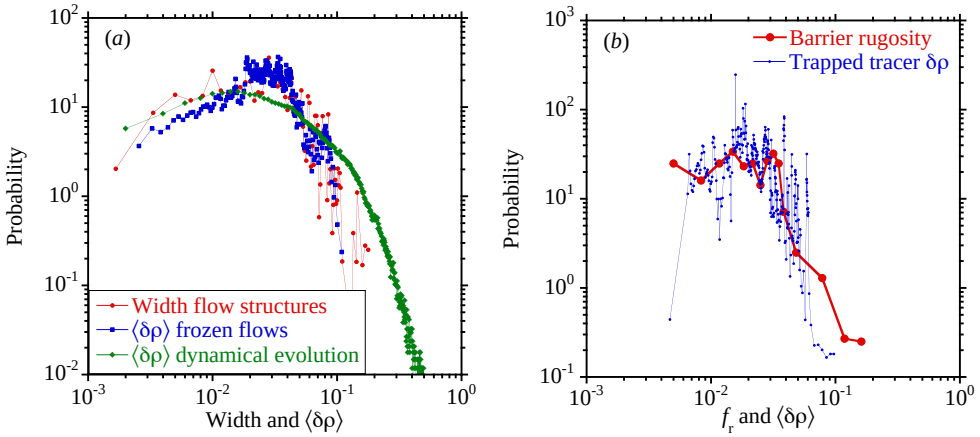

Figure 14. For case 2: (a) PDF of $\langle\delta\rho\rangle$ for $V_0 = 50$ (frozen and evolving fields) for tracers verifying the trapping condition in equation (15) and the PDF of the width of the structures. (b) $\langle\delta\rho\rangle$ for the other trappings and the PDF of the rugosity of the barriers.

FIG14

of the width and rugosity of the structures have poorer resolution.

For the case of toroidal geometry, case 4 in Table 1, the situation is somewhat different. The PDF of $\langle\delta\rho\rangle$ is the same for all the velocities considered as in previous cases. This can be seen in figure 15(a). However, the comparison between the PDF of the width of the flow structures and the PDF of $\langle\delta\rho\rangle$ for the trapped tracers is not as good as the previous cases. In figure 15(b) we show this comparison and we can see clear discrepancies.

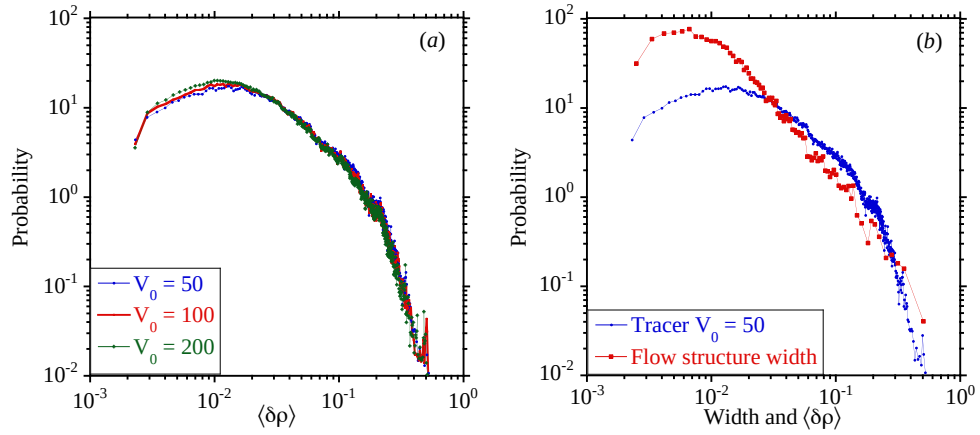

Figure 15. (a) PDF of the $\langle\delta\rho\rangle$ of the tracers for three values of the parallel velocity, (b) PDF of $\langle\delta\rho\rangle$ for $V_0 = 50$ and the PDF of the width of the flow structures for case 4.

FIG15

The reason for this discrepancy is simple. In the toroidal case, not only we have vortices and merging between two or three that are close to each other but we also have streamers. They are long structures that link the interior of the plasma to the edge by merging many vortex structures. These flow structures can be clearly seen in

figure 3, case 4. In general, these long streamers do not trap the tracers. In most of the cases, tracers following those streamers just leave the plasma in a single flight.

If we add to the $\langle \delta\rho \rangle$ from the trapped tracers the single flights, then we have a different type of PDF. In figure 16, we show this combined PDF. This PDF has a power law tail and the exponent associated to this tail is -1.82, very close to the value of the exponents for the tail of the PDF of the width of flow structures given in Table 3.

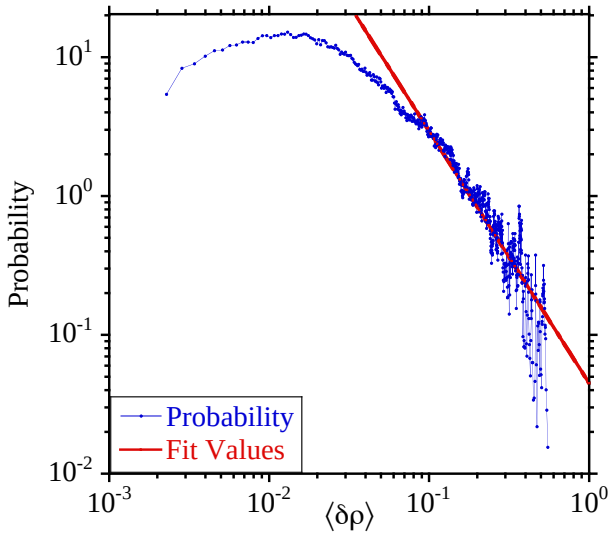

FIG16

Figure 16. (a) PDFs of the $\langle \delta\rho \rangle$ of the trapped tracers and single flights for case 4.

So in this case, the flow structures do not give us the separation between the trappings and the flights out of the plasma. We should look for the toroidal case instabilities that are more localized than the resistive MHD modes in order to identify better the trapping structures.

6. Conclusions

sec:Conclusions

Resistive pressure-gradient-driven turbulence offers a variety of features depending on the geometry and characteristic properties of the global flows. The investigation of simple geometry configurations is helpful in identifying main features of the flow structures and the correlations between flow structures and tracers which help in later analyzing more realistic situations.

In cylindrical geometry, the radial width of the flow structures follows a lognormal distribution. However, in toroidal geometry, the distribution has a power tail of exponent close to 2. This is a qualitative distinction with potential impact on transport.

The effect of the global shear flow in the cylindrical geometry cases is: 1) to create potential barriers, 2) to reduce the number of localized flow structures and 3) to reduce the width of the remaining flow structures.

We also found a clear correlation between the radial extend of the flow structures and the radial excursions of the tracer particles during their trapping phase. The

character of trapping may change with the magnetic field geometry and by the presence of an averaged flow.

Without an averaged flow and in cylindrical geometry, tracers are trapped by vortex type flow structures and the radial excursions during the trapping correlate well with the widths of these vortex structures.

When an averaged poloidal flow is generated, there are two types of trapping, one by the vortex structure and another by the mini-transport barriers. For the cases that trapping is by vortex structure, the radial excursion of the tracer is directly related to the width of this vortex. However, in the case that the tracer is trapped by a barrier, the radial excursions are given by the roughness of the barrier. The rugosity parameter that we have introduced here to characterize the barrier gives a good correlation with the radial excursions of the trapped tracers.

In the toroidal case, the presence of streamers does not allow to separate between flow structures responsible for trapping of the tracers and flow structures that lead tracers out. However, the flow structures are still consistent with the tracers' flights. We need to investigate more localized toroidal instabilities to better identify the flow structures responsible for trapping.

Before constructing a transport theory based on the CTRW approach, we need to investigate the trapping times of the tracers and their relation to properties of the flow structures. For that will possibly be important the lifetime of the cycles and the length of broken filaments. All these properties need to be quantified for the different magnetic geometries.

Appendix A. Parameters of the magnetic configurations

sec:Conf

For cases 1, 2 and 3 from Table 1, the plasma considered here is a model of a configuration of the Large Helical Device (LHD) [16]. The q-profile is

$$q(r) = 2.726 - 3.3r^2 + 1.7r^4 - 0.48r^6 \tag{A.1}$$

The LHD plasma has bad averaged curvature, which we model by

$$\kappa_r(r) = -\frac{1}{2a}\left(0.296r + 1.712r^3 + 4.854r^5 + 5.936r^7\right) \tag{A.2}$$

and the equilibrium pressure profile by

$$p_{eq}(r) = p_{eq}(0)(1 - r^4)\left(1 - \frac{r^2}{2}\right) \tag{A.3}$$

In these expressions, the radius r is normalized to the minor radius a.

The main parameters of the nonlinear calculation are: $\beta_0 = 0.0044$, the inverse aspect ratio $\varepsilon = a/R_0 = 0.163$ and the Lundquist number $S = \tau_R/\tau_A = 10^5$. For these parameters, this configuration is unstable to resistive interchange modes. Here, β_0 is the ratio of the plasma pressure and the magnetic pressure at the plasma axis, $\beta_0 = 2\mu_0 p(0)/B_0^2$, τ_R is the resistive time, $\tau_R = \mu_0 a^2/\eta$, where η is constant, and τ_A is the Alfvén time, $\tau_A = R_0\sqrt{\mu_0 m_i n_i}/B_0$.

In the numerical calculations, we use the previously discussed Fourier expansion. A broad spectrum of modes is generated when the turbulence reaches a steady state. We included 3785 modes with m going up to $m = 85$. The radial grid is uniform and $\Delta r = 10^{-3}$.

For case 4 from Table 1 (toroidal configuration), the parameters used in the calculations correspond to a medium-size tokamak with circular cross section [17].

As initial condition for the calculations, a tokamak equilibrium solution is calculated using the Grad-Shafranov equation. We use as input in the equilibrium calculations a pressure and safety factor with

$$p_{eq}(\rho) = p_{eq}(0)\left[1 - \frac{\psi(\rho)}{\psi(1)}\right]^2 \tag{A.4}$$

and

$$q(\rho) = 0.9\left[1 + \left(\frac{\rho}{0.6521}\right)^4\right]^{1/2} \tag{A.5}$$

where ρ is normalised to 1 at the edge.

The main parameters of the nonlinear calculation are: $\beta_0 = 0.01$, the inverse aspect ratio $\varepsilon = 0.25$ and the Lundquist number $S = 10^5$. For these parameters, this configuration is unstable to resistive ballooning modes in the outer half region of the minor radius. In the numerical calculations, we included 8187 modes with n going up to $n = 119$. The radial grid is nonuniform and $\Delta\rho = 5 \times 10^{-4}$ for $\rho > 0.5$.

Acknowledgments

This research was sponsored by DGICYT (Dirección General de Investigación Científica y Técnica) of Spain under Project No. ENE2012-38620-C02-02. One of us (BAC) also gratefully acknowledges the support from a "Cátedra de Excelencia" from Universidad Carlos III and Banco de Santander.

References

Doyle [1] E J Doyle et al. Progress in the ITER Physics Basis Chapter 2: Plasma confinement and transport 2007 *Nucl. Fusion* **47** S18

Montroll [2] Montroll E.W. and Weiss G. 1965 *J. Math. Phys.* **6** 167

Carreras3 [3] Carreras B.A., Llerena Rodríguez I. and García L. 2013 *J. Phys. A: Math. Theor.* **46** 375501

Carreras5 [4] Carreras B.A., Llerena Rodríguez I. and García L. 2014 *Nucl. Fusion* **54** 103005

Vlad [5] Vlad M., Spineanu F., Misguich J.H. and Balescu R. 2002 *Nucl. Fusion* **42** 157

Basu [6] Basu R., Jessen T., Naulin V. and Rasmussen J.J. 2003 *Phys. Plasmas* **10** 2696

Hauff [7] Hauff T. and Jenko F. 2007 *Phys. Plasmas* **14** 092301

Carreras2 [8] Carreras B.A., Lynch V.E. and Zaslavsky G.M. 2001 *Phys. Plasmas* **8** 5096

McNaught [9] IUPAC. Compendium of Chemical Terminology, 2nd ed. (the "Gold Book"). Compiled by A. D. McNaught and A. Wilkinson. Blackwell Scientific Publications, Oxford (1997)

Friedman [10] Friedman A., Pizarro O., Williams S.B., Johnson-Roberson M. 2012 *PloS ONE* **7** e50440

Strauss [11] Strauss H.R. 1977 *Phys. Fluids* **20** 1354

Garcia2 [12] Garcia L., Carreras B.A. and Lynch V.E. 1999 *Phys. Plasmas* **6** 107

Biglari [13] Biglari H., Diamond P.H. and Terry P.W. 1990 *Phys. Fluids* B **2** 1

Clauset [14] Clauset A., Shalizi C.R. and Newman M.E.J. 2009 *SIAM Review* **51** 661

Shampine [15] L.F. Shampine and M.K. Gordon, Computer solution of ordinary differential equations: the initial value problem (W.H. Freeman, San Francisco, 1975)

Iiyoshi [16] Iiyoshi A. et al. 1999 *Nucl. Fusion* **39** 1245

Garcia [17] Garcia L. and Carreras B.A. 2006 *Phys. Plasmas* **13** 022310